

Article

Effect of In-Situ H Doping on the Electrical Properties of In₂O₃ Thin-Film Transistors

Peixuan Hu^{1,2}, Zhixiang Gao², Lu Yang², Wanfa Li², Xiaohan Liu^{1,2}, Ting Li^{1,2}, Yujia Qian^{1,2}, Lingyan Liang^{2,*}, Yufang Hu¹  and Hongtao Cao^{2,*}

- ¹ State Key Laboratory Base of Novel Functional Materials and Preparation Science, School of Materials Science and Chemical Engineering, Ningbo University, Ningbo 315211, China; hupeixuan@nimte.ac.cn (P.H.); liuxiaohan@nimte.ac.cn (X.L.); liting@nimte.ac.cn (T.L.); qianyujia@nimte.ac.cn (Y.Q.); huyufang@nbu.edu.cn (Y.H.)
- ² Laboratory of Advanced Nano Materials and Devices, Ningbo Institute of Materials Technology and Engineering, Chinese Academy of Sciences, Ningbo 315201, China; zxgao@mail.ustc.edu.cn (Z.G.); yjhylyh814915@163.com (L.Y.); lwf078@mail.ustc.edu.cn (W.L.)
- * Correspondence: lly@nimte.ac.cn (L.L.); h_cao@nimte.ac.cn (H.C.)

Abstract: In this article, this research demonstrates the influence of in-situ introduction of H₂ into the working gas on the physical properties of post-annealed In₂O₃ thin films and the performance of associated devices. A gradual increase in the H₂ ratio leads to improved film quality, as indicated by spectroscopic ellipsometry, X-ray photoelectron spectroscopy, and atomic force microscope analyses showing a reduction in defect states such as band-tail states and V_O in the film, and a smoother surface morphology with the root mean square roughness approximately 0.446 nm. Furthermore, this hydrogen doping effect results in a distinct shift in the device's threshold voltage toward the positive direction, and an improvement in the field-effect mobility and subthreshold swing. Consequently, a high-performance In₂O₃:H TFT is developed, exhibiting a field-effect mobility of 47.8 cm²/Vs, threshold voltage of −4.1 V and subthreshold swing of 0.25 V/dec. These findings highlight the potential of in-situ H doping as a promising approach to regulate In₂O₃-based TFTs.

Keywords: thin-film transistors; metal oxide semiconductors; hydrogen; mobility; flat-panel displays



Citation: Hu, P.; Gao, Z.; Yang, L.; Li, W.; Liu, X.; Li, T.; Qian, Y.; Liang, L.; Hu, Y.; Cao, H. Effect of In-Situ H Doping on the Electrical Properties of In₂O₃ Thin-Film Transistors.

Electronics **2024**, *13*, 1478. <https://doi.org/10.3390/electronics13081478>

Academic Editor: Francesco Giuseppe Della Corte

Received: 14 March 2024

Revised: 9 April 2024

Accepted: 11 April 2024

Published: 13 April 2024



Copyright: © 2024 by the authors. Licensee MDPI, Basel, Switzerland. This article is an open access article distributed under the terms and conditions of the Creative Commons Attribution (CC BY) license (<https://creativecommons.org/licenses/by/4.0/>).

1. Introduction

Since the report by Nomura et al. on thin-film transistors (TFTs) using InGaO₃(ZnO)₅, oxide semiconductors (OSs) have been extensively researched due to their promising properties, such as wide band gap, excellent electrical properties, simple preparation, and good compatibility with Si-based manufacture. OSs have emerged as exceptional candidates for TFTs in pixel switching/driving applications for flat-panel displays (FPDs) [1]. However, while driving ultra-high-resolution FPDs at high frame rates, the field-effect mobility (μ_{FE}) of oxide TFTs needs to be improved further [2]. In addition, other properties such as threshold voltage (V_{th}) and TFT stability are also critical factors that should be considered simultaneously [3]. Hence, it is essential to explore new OSs or fabrication techniques to improve the performance of OS TFTs.

Prototype OS materials used in TFT devices are indium oxide (In₂O₃), tin oxide (SnO₂), and zinc oxide (ZnO). Among them, In₂O₃-based OSs are considered as the most promising materials to achieve high mobility. Firstly, the conduction band bottom of In₂O₃ is composed of the 5s orbitals of the indium ion with a large orbital radius and a high overlap, which provides a highway for electron transportation [4,5]. Secondly, theoretical calculations show that In₂O₃ has a small and isotropic effective mass of electrons (0.22 m_0) [6]. Finally, some theories suggested that a higher In content results in a larger average effective coordination number of M–O bonds and more corner-, edge-, and face-shared M–O polyhedrons, which enhances overlapping of electron wavefunctions [3].

However, the excessively high carrier concentration (generally larger than 10^{18} cm^{-3}) of In_2O_3 makes it challenging to adjust electrical properties [4,7]. In order to regulate the electrical performance of In_2O_3 -based TFTs, researchers have been studying extensively the effect of doping, which is considered to be the most promising method due to its effectiveness and simplicity.

Dopants can be categorized into cation and anion elements. In the case of cation doping, dopants with elements such as Ti, Hf, Zr, Bi, and W that have high oxygen bond dissociation energies, suppressed the concentration of excess oxygen vacancies (V_{O}), and then reduced the electron concentration in the films and improved the stability of the device [8–12]. Doping with lanthanide elements, such as Pr and Tb, shortened the relaxation time of photo-generated electrons and then enhanced the device's stability [13,14]. However, it should be noted that those cation dopants tend to have a somewhat degrading effect on the μ_{FE} of TFTs. On the other hand, anionic dopants like N, F, and H were also introduced to tune the film and the device's performance. It was found that nitrogen doping could enhance the device's stability by suppressing V_{O} and other trap states [15,16], while fluoride could passivate V_{O} , suppress the formation of free carriers, and then improve stability [17–19]. And there are also a few reports on hydrogen doping. Wardenga et al. prepared H-doped In_2O_3 thin films ($\text{In}_2\text{O}_3:\text{H}$) by RF magnetron sputtering and found that hydrogen passivation of grain boundaries was the main reason for the high mobility observed in $\text{In}_2\text{O}_3:\text{H}$ films [20]. Magari et al. conducted a study on anion doping with H and found that it plays a crucial role in increasing grain size and decreasing subgap defects, leading to an enhanced μ_{FE} [21]. In summary, it mainly contributed the μ_{FE} improvement to H-induced grain growth. Therefore, it is essential to further investigate H doping in In_2O_3 , to supply more information on its effect on the film and device properties, such as the film microstructure, device μ_{FE} , device threshold voltage (V_{th}), and others.

In this work, In_2O_3 and $\text{In}_2\text{O}_3:\text{H}$ films were deposited by magnetron sputtering and their physical properties were investigated as a function of the H_2 ratio in the working gas. The results show that increasing the introduction of H_2 induces no grain growth, widens the band gap, makes the absorption edge steeper, and increases the percentage of M-O bonds. These variations correspond to a clear reduction in the electron concentration in In_2O_3 . As a result, the TFT V_{th} obviously shifts to the positive direction and the μ_{FE} is also improved with increasing H_2 ratio, showing that H doping is a promising way to regulate In_2O_3 -based TFTs.

2. Experimental Methods

Heavily p-type doped Si wafers and 100 nm-thick SiO_2 were utilized as the gate electrode and insulator, respectively. The 25 nm In_2O_3 and $\text{In}_2\text{O}_3:\text{H}$ channels were deposited using a 2-inch diameter In_2O_3 ceramic target (99.99% purity) through RF magnetron sputtering in a mixture of Ar, O_2 , and H_2 gases at room temperature (RT). The O_2 and H_2 gas flow ratios are denoted as $R[\text{O}_2] = \text{O}_2 / (\text{Ar} + \text{O}_2 + \text{H}_2)$ and $R[\text{H}_2] = \text{H}_2 / (\text{Ar} + \text{O}_2 + \text{H}_2)$, respectively. For the In_2O_3 and $\text{In}_2\text{O}_3:\text{H}$ film, $R[\text{O}_2]$ was constant at 2.5%, $R[\text{H}_2]$ was set to 0, 3, and 5%. The films were annealed at 350 °C for 1 h in air, and then a 100 nm-thick Al source/drain (S/D) layer was deposited through the direct current (DC) magnetron sputtering method using pure Ar gas at an input power of 65 W. The In_2O_3 and Al films were patterned using two different shadow masks. The width/length (W/L) was 800 μm /400 μm . Finally, the fabricated TFTs were annealed at 250 °C for 1 h in air. The optical absorption coefficient of the films was obtained through spectroscopic ellipsometry analysis (SE, M-2000 DI, J. A. Woollam, Lincoln, NE, USA), and the films' structural changes and crystallinity were evaluated via X-ray diffraction (XRD, D8 ADVANCE DAVINCI, Bruker, Karlsruhe, DE, USA) and transmission electron microscopy (TEM, Talos F200X, Thermo Fisher, Waltham, MA, USA). Surface morphology of the films was observed using an atomic force microscope (AFM, Dimension ICON, Bruker, Billerica, MA, USA). Hall effect testing was employed to determine various electrical properties of the thin films (8404-CRX-6.5K, Lake Shore, Woburn, MA, USA), whereas X-ray photoelectron spectroscopy (XPS, AXIS ULTRA DLD, Shimadzu, Kyoto, Japan) was utilized to investigate

internal properties and bonding character. A Keithley 4200SCS semiconductor parameter analyzer was employed to determine the electrical characteristics of the TFT devices.

3. Results and Discussion

Figure 1a displays the XRD patterns in θ - 2θ scans of 50 nm-thick unannealed In_2O_3 films with varying $R[\text{H}_2]$. The XRD spectra of as-deposited In_2O_3 films presented low diffraction intensity and rather broad background, indicating that the as-deposited films produced through magnetron sputtering are amorphous. After annealing in air at 350 °C for 1 h, all the films turn to the polycrystalline state; as observed in Figure 1b, there are four clear characteristic peaks which correspond to the (222), (400), (440), and (662) crystal planes [22]. These observed diffraction lines agree well with the cubic bixbyite indium oxide structure (JCPDS06-0416) and $Ia-3$ space group (Number: 206). Calculated with Scherrer's formula on the reflection (222), the grain sizes of the In_2O_3 films with 0%, 3%, and 5% hydrogen content are determined to be 50.6 nm, 48.2 nm, and 49.5 nm, respectively. Interestingly, as $R[\text{H}_2]$ increases, the intensity of the (222) peak gradually lowers. These results indicate that the introduction of H in In_2O_3 does not promote grain growth, while it even more or less suppresses the crystallinity [23]. It is worth mentioning that these observations diverge from existing reports on H-doped In_2O_3 [21], which may be attributed to the discrepancy in the phases of the as-deposited In_2O_3 films: polycrystalline in the literature and amorphous in this work.

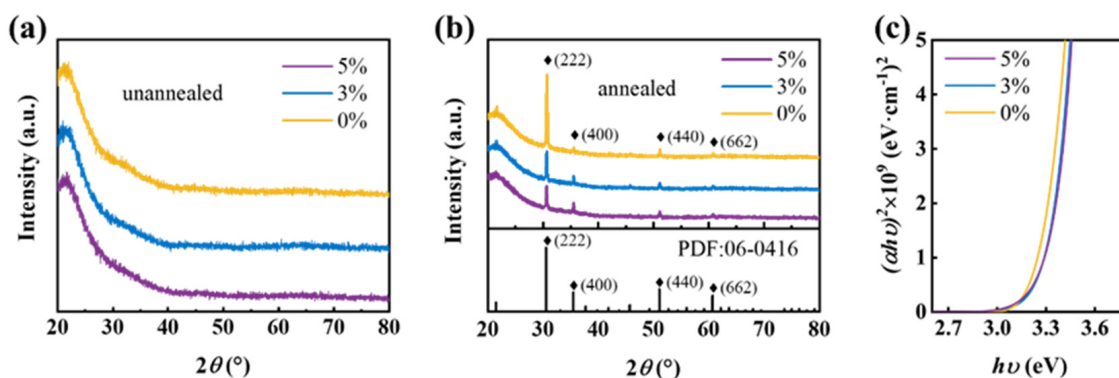


Figure 1. XRD patterns of the In_2O_3 and $\text{In}_2\text{O}_3:\text{H}$ films deposited at different $R[\text{H}_2]$ and at a constant $R[\text{O}_2]$ value of 2.5% (a) before and (b) after annealing at 350 °C in air. Inset: (bottom) standard XRD spectra of In_2O_3 . (c) Plots of $(\alpha hv)^2$ versus hv of the annealed In_2O_3 and $\text{In}_2\text{O}_3:\text{H}$ films.

Figure 1c presents the optical band gap (E_g) of the annealed films, which is estimated by the Tauc method ($\alpha hv \sim (hv - E_g)^n$) [24]. Since In_2O_3 has a direct band gap [25], then $n = 1/2$ and thus hv is estimated by extrapolating the linear $(\alpha hv)^2$ edge, where hv represents the incident photon energy and α is the absorption coefficient obtained by spectroscopic ellipsometry analysis. The optical band gaps of In_2O_3 thin films are mostly reported in the range of 2.9–3.8 eV [7,23,25–28]. The calculated E_g values of the $\text{In}_2\text{O}_3:\text{H}$ films are very similar: about 3.28 eV, which is slightly larger than that of the In_2O_3 film (3.23 eV). And it can be observed that the absorption edges of the $\text{In}_2\text{O}_3:\text{H}$ films are clearly steeper than that of the In_2O_3 film. These imply that the addition of hydrogen may be able to reduce the band-tail defects in In_2O_3 , although it decreases the crystallinity of the In_2O_3 film.

In order to verify the crystallinity of the film, four representative samples were selected as undoped In_2O_3 and $\text{In}_2\text{O}_3:\text{H}$ films with the highest doping concentration ($R[\text{H}_2] = 5\%$) in the as-deposited and annealed states, respectively. The cross-sectional HR-TEM images of the four representative samples are presented in Figure 2a–d. For the as-deposited samples, the films exhibit an amorphous structure, consistent with the Fast Fourier Transformed results (inserts in Figure 2a,c), revealing diffused hollow rings indicative of the amorphous phase. Upon annealing, distinct grain boundaries and diffraction stripes were observed in Figure 2b,d. The domain-spacing (d-spacing) of the two labeled spherical particles in

the (222) crystal plane is about 2.91 and 2.84 Å, respectively, which is consistent with the standard cubic bixbyite-type structure of In_2O_3 (JCPDS06-0416). These results are in line with the results from the XRD test.

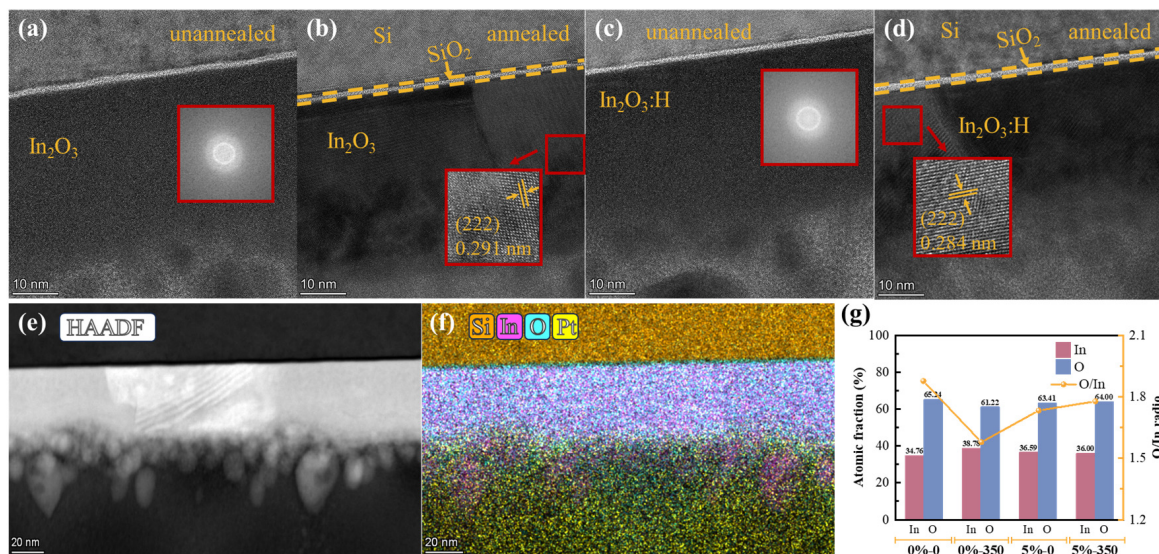


Figure 2. Cross-sectional HR-TEM images (a) 0%-0, (b) 0%-350, (c) 5%-0, (d) 5%-350. The insets to (a,c) show the Fast Fourier Transformed images of the as-deposited films. (e) HAADF image and (f) EDS mapping results of the annealed $\text{In}_2\text{O}_3\text{:H}$ films at $R[\text{H}_2] = 5\%$. (g) Atomic fractions of In, O, and the O/In ratios in as-deposited and annealed In_2O_3 and $\text{In}_2\text{O}_3\text{:H}$ films obtained from EDS analysis.

Figure 2e exhibits the high-angle angular dark-field (HAADF) image of $\text{In}_2\text{O}_3\text{:H}$ films ($R[\text{H}_2] = 5\%$); the interface between the Si layer and In_2O_3 layer is distinct and sharp. The thickness of the In_2O_3 layer is measured to be approximately 47.8 nm. This result is in good agreement with the simulated thickness which obtains from the spectroscopic ellipsometry analysis. One may also observe some large particles at the Pt region, which makes the $\text{In}_2\text{O}_3/\text{Pt}$ interface unclear. These particles can be observed on all the samples chosen for TEM testing. Figure S1a shows the HAADF image of the as-deposited $\text{In}_2\text{O}_3\text{:H}$ films at $R[\text{H}_2] = 5\%$, where the particles are larger and their details are clearer compared to Figure 2c. EDS element analysis, shown in Figure S1b, shows that the element distribution of these large particles is indium-rich and oxygen-poor, which is the opposite of the element content inside the film. The atomic fractions (%) of Pt, O, and In are 2.78%, 25.89%, and 71.33%, respectively. By combining the two figures, it can be clearly observed that those large particles are separated from the indium oxide film region, seemingly suspended on the surface of this sample. This is because there is a distinct boundary between the particles and the In_2O_3 region, and the boundary is dominated with Pt. Figure 2f illustrates the corresponding energy-dispersive spectrometer (EDS) mapping for Si, In, O, and Pt elements, which reveals the homogeneous distribution of all elements. The In and O elements in the representative sample film were analyzed and the O/In ratio was calculated, as shown in Figure 2g. The results indicate minimal variation in the content of In and O across all samples. The O/In ratios of the hydrogen-doped films exhibit minimal change before and after annealing, in stark contrast to the undoped films. For the undoped films, upon thermal annealing at 350 °C, both the O content and the O/In ratios decrease and the V_{O} increase, implying that some O atoms escape from their lattice positions, which is a frequent reported phenomenon for metal oxide semiconductors [29–31]. Conversely, in the case of H-doped films, the O/In ratios remain statistically unchanged between the as-deposited and annealed states. It is suggested that the introduction of hydrogen during the sputtering process may be the underlying cause of this phenomenon, as it significantly enhances the films' ability to fix oxygen. It has been mentioned in the literature that as the temperature

increases, the unstable interfacial In-H-In defects release hydrogen, which in turn combines with oxygen to form stronger covalent bonds, such as In-OH [32,33]. Furthermore, the O/In ratios of the annealed In_2O_3 film are observed to be lower than that of the annealed $\text{In}_2\text{O}_3:\text{H}$ film.

Figure 3 shows the topographic profiles obtained by AFM scanning on both the as-deposited and annealed films at different hydrogen concentrations. A high-pass filter was applied to remove the swelling component on the substrate. The root mean square (RMS) roughness calculated from the AFM image is also displayed in Figure 3. The RMS values of the as-deposited films with hydrogen concentration of 0%, 3%, and 5% are 0.467, 0.350, and 0.307 nm, respectively. Notably, the test results reveal a gradual reduction in roughness with the introduction of hydrogen during the deposition process. After thermal annealing at 350 °C, the images showed that the surface morphology of In_2O_3 and $\text{In}_2\text{O}_3:\text{H}$ thin films had undergone significant alterations, aligning well with the findings derived from XRD analysis. During the annealing process, the grains gradually aggregate to form grain clusters, and obvious boundaries are formed around the clusters. And the surface morphology of the undoped In_2O_3 film after annealing bears resemblance to the texture of a Hami melon peel. Compared with the annealed In_2O_3 film, the boundary surrounding the crystal clusters in the $\text{In}_2\text{O}_3:\text{H}$ films becomes shallower, and the surface is notably smoother.

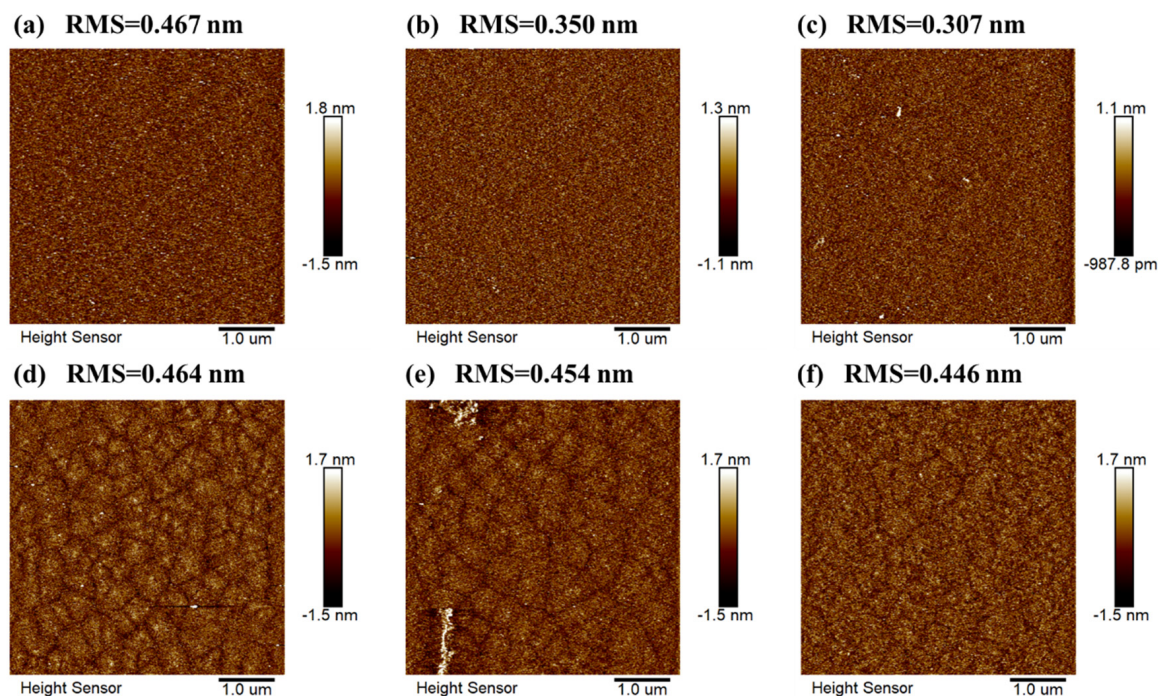


Figure 3. AFM images and root mean square roughness RMS (a) 0%-0, (b) 3%-0, (c) 5%-0, (d) 0%-350, (e) 3%-350, (f) 5%-350.

To further investigate the effect of hydrogen, XPS measurements were conducted. Considering that water, carbon, and other impurity molecules in the air will be adsorbed onto and even into the sample, a high dose of argon ions, specifically with an ion energy of 2 KeV and a current density of roughly $5 \mu\text{A}/\text{cm}^2$, was applied to sputter away the top surface layer (about 20 nm), while the total thickness of the sample was 50 nm. Figure 4a–c shows the O 1s spectra for the inner layer of the annealed films. They are calibrated by taking the binding energy of the C 1s peak (284.8 eV) as a reference. Gaussian fitting is employed to deconvolute the O 1s peaks. The lowest binding energy Gaussian peak (O_L) at 529.8 eV originates from metal–oxygen bonds (M–O lattice); the peak at the middle binding energy 530.7 eV (O_M) is linked to O^{2-} ions of oxygen defects, such as V_O ; while the highest binding energy Gaussian peak (O_H) at 531.9 eV is usually associated with specific chemisorbed oxygen such as $-\text{CO}_3$, $-\text{OH}$, and H_2O [34–36]. The area percentages of the

three O peaks were calculated and are summarized in Table 1. It was found that with increasing R[H₂], the percentage of M-O bonds (O_L) increases while the recent part related to the defects and impurities (O_M and O_H) decreases. This implies that in-situ H doping in the deposition of In₂O₃ film aids in improving film quality during the post-annealing process, especially by reducing V_O or other impurity defects. It is also consistent with the EDS element content analysis that the In₂O₃:H film has less V_O than the In₂O₃ film, which has higher oxygen content and a higher O/In ratio.

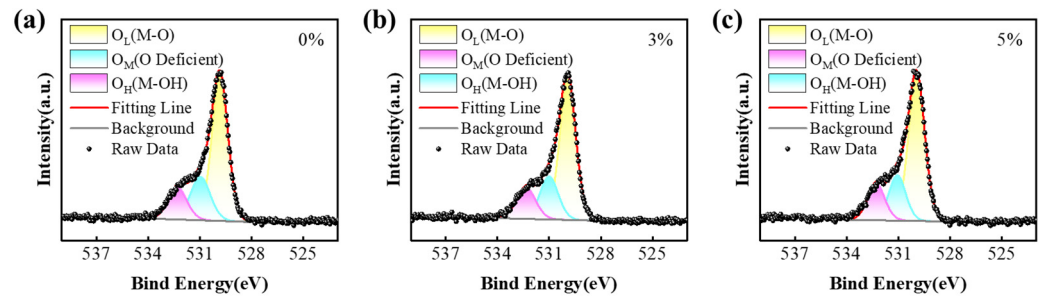


Figure 4. The XPS O 1s spectroscopic analysis of In₂O₃ etching films at a depth of 20 nm with different R[H₂]: (a) R[H₂] = 0%; (b) R[H₂] = 3%; (c) R[H₂] = 5%.

Table 1. The percentage of O 1s peak area in XPS spectra and Hall effect testing results of the films.

	In-O (%)	V _O (%)	Impurity Molecules (%)	μ _H (cm ² /Vs)	N _e (1/cm ³)	ρ (Ω·cm)
0%	61.32	20.46	18.22	14.3	7.46 × 10 ¹⁷	0.586
3%	62.68	19.74	17.59	18.0	4.64 × 10 ¹⁶	7.49
5%	63.95	18.76	17.29	18.0	6.53 × 10 ¹⁶	5.31

To investigate the electrical properties of the annealed In₂O₃ and In₂O₃:H films, Hall effect measurement was employed to determine the Carrier Hall mobility (μ_H), electron concentration (N_e), and resistivity (ρ) of the thin films. The summarized data are presented in Table 1. The undoped film exhibits a low ρ (0.586 Ω·cm) and a relatively high N_e of 7.46 × 10¹⁷/cm³. Upon the introduction of H, the ρ increases by at least one order of magnitude, which mainly originates the decrease in the N_e, down to 4.64 × 10¹⁶/cm³ at R[H₂] = 3% and 6.53 × 10¹⁶/cm³ at R[H₂] = 5%. Additionally, the μ_H increased from 14.3 cm²/Vs for the In₂O₃ film to 18.0 cm²/Vs for the In₂O₃:H film. These variations imply that there are fewer donor defects available to provide free electrons in the In₂O₃:H films compared to the undoped In₂O₃ film. These findings also agree well with the results obtained from absorption spectra and XPS analysis that V_O and band-tail states are clearly reduced by H doping, since these two kinds of defects are highly associated with donor states near the conduction band minimum of OSs. And the reduction in these defect states also brings an increase in mobility due to the reduction in carrier scattering centers. In addition, a smoother surface morphology also plays a role in improving the mobility of the device.

The fabricated In₂O₃-based TFTs' device structure is depicted in Figure 5a. The transfer characteristics of all annealed TFTs, displayed in Figure 5b, were measured at room temperature with a drain-source voltage (V_{DS}) of 10.1 V. V_{th} was defined by gate voltage (V_{GS}) at a drain current (I_D) of 10 nA, and SS was extracted from V_{GS}, which required an increase in the I_D average values from 0.1 nA to 10 nA. It is evident that as the R[H₂] gradually increases, the V_{th} of the TFTs significantly shifts toward the positive direction. Specifically, the V_{th} changes from −15.0 V to −4.1 V. This observed shift in V_{th} corresponds well with the decrease in N_e of the films, as determined by the Hall measurement. What is more, the μ_{FE} of the device also exhibits an improvement trend with increasing R[H₂]. Herein, the μ_{FE} is derived from the transfer curves measured at V_{DS} = 10.1 V, where the devices are working in the saturation region (as seen in the output

curves of Figure 5c). The μ_{FE} values increase from $37.8 \text{ cm}^2/\text{Vs}$ to $47.8 \text{ cm}^2/\text{Vs}$, which is in good accordance with the corresponding trend observed for the μ_H . It is worth noting that the μ_{FE} values are larger than the μ_H values due to the special carrier transportation mechanism corresponding to the percolation theory for OSs [37]. In TFTs, as the gate voltage increases, localized states become occupied with gate-induced carriers, causing the Fermi level (E_F) to shift toward the mobility edge (E_m). In such scenarios, the occupied localized states do not trap additional electrons. Particularly when the gate-induced carriers occupy a significant portion of the localized states and the electron density in the channel is sufficiently high to elevate the E_F above E_m , electrons can move more freely, resulting in higher mobility compared to intrinsic films with lower N_e . As a result, the electrons can move relatively freely, leading to a higher mobility compared to the intrinsic films with lower N_e . Figure 5c shows the output characteristics of In_2O_3 ($R[\text{H}_2] = 0\%$), $\text{In}_2\text{O}_3:\text{H}$ ($R[\text{H}_2] = 3\%$), and $\text{In}_2\text{O}_3:\text{H}$ ($R[\text{H}_2] = 5\%$) devices. The I_D increases linearly at the region of low source-drain voltage (V_{DS}), indicating that an Ohmic contact formed between the S/D electrodes and channel layer. Clear pinch-off and saturation characteristics are evident in the saturation region of the output curve, indicating effective control of the transistor channel by the gate and source/drain. $\text{In}_2\text{O}_3:\text{H}$ TFTs all exhibit high levels of output curve saturation current ($V_{DS} = 15 \text{ V}$, $I_D = 587 \mu\text{A}@V_{GS} = 15 \text{ V}$ at $R[\text{H}_2] = 3\%$, $I_D = 560 \mu\text{A}@V_{GS} = 12 \text{ V}$ at $R[\text{H}_2] = 5\%$). The I_D of In_2O_3 TFT without introducing H_2 is decreased to $361 \mu\text{A}$ ($V_{GS} = 1 \text{ V}$, $V_{DS} = 15 \text{ V}$). It shows that with the addition of hydrogen, the TFT exhibits excellent current amplification performance.

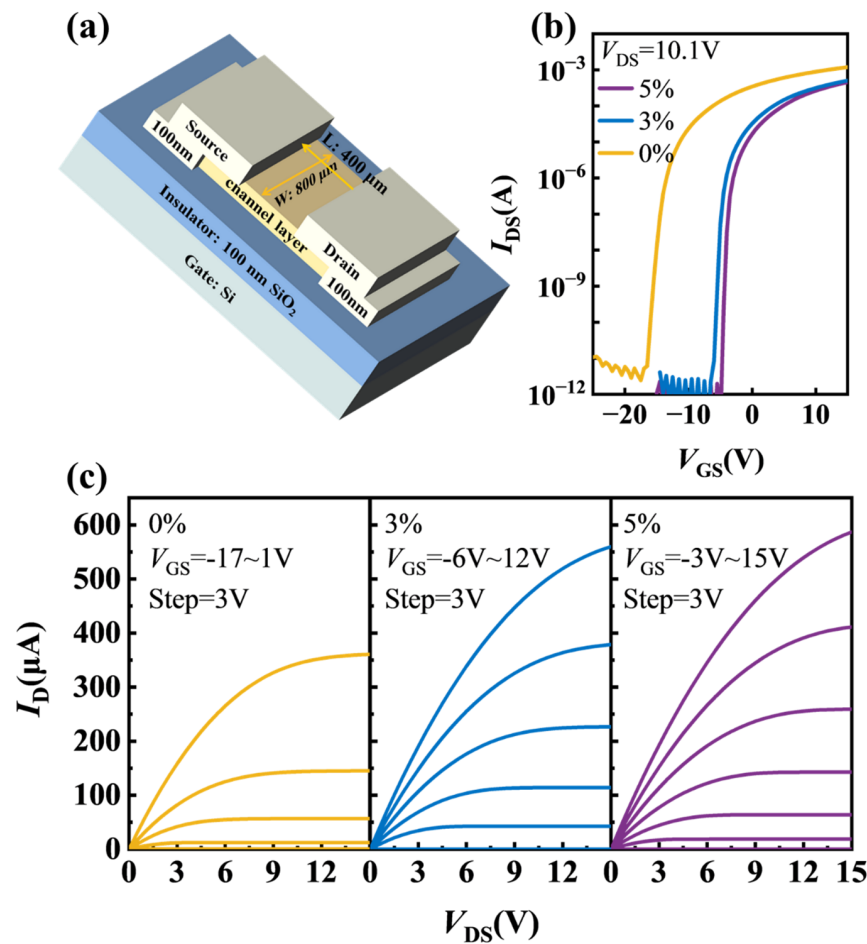


Figure 5. (a) Schematic view of a TFT device. (b) Typical transfer characteristics ($V_{DS} = 10.1 \text{ V}$) for all devices with In_2O_3 and $\text{In}_2\text{O}_3:\text{H}$ channels deposited at various $R[\text{H}_2]$ values. (c) Typical output curves of the TFTs.

In addition, as depicted in Figure 5b and detailed in Table 2, the off-state current (I_{off}) of the device subjected to the in-situ hydrogen doping process is significantly lower compared to that of the undoped device. As a result, the on-off current ratio ($I_{\text{on}}/I_{\text{off}}$) of the device shows a notable improvement, increasing specifically from 2.83×10^7 ($R[\text{H}_2] = 0\%$) to 7.20×10^8 ($R[\text{H}_2] = 5\%$), where the I_{on} refers to the current value at $V_{\text{GS}} = 15$ V on the transfer curve. These improvements can sensitively reflect changes in the channel defect states. It is worth noting that there is a distinct improvement in subthreshold swing (SS) from 0.52 V/dec to 0.25 V/dec after in-situ H doping. The SS is generally considered as an indicator of the sum of the defect states in oxide semiconductors and semiconductor/dielectric interface trap states. In this context, we introduce the concept of an effective maximum areal density of states, denoted as N_{eff} , which is calculated using the following formula [38]:

$$N_{\text{eff}} = \left(\frac{SS \log(e)}{kT/q} - 1 \right) \frac{C_{\text{ox}}}{q} \quad (1)$$

where k represents the Boltzmann constant, T is the temperature, q is the electron charge, and C_{ox} denotes gate oxide capacitance per unit area. The N_{eff} were calculated to be 1.82×10^{12} , 9.46×10^{11} , and 8.76×10^{11} cm^{-2}/eV for In_2O_3 TFTs deposited at $R[\text{H}_2] = 5\%$, 3% , and 0% , respectively. These results indicate that an increase in $R[\text{H}_2]$ leads to a reduction in the N_{eff} of the device. Since the dielectrics and fabrication conditions used are the same just with H doping, it is believed that the semiconductor/dielectric interface trap states are very similar for the three devices, and the decrease in the N_{eff} should correspond to the reduction in the defect states in oxide semiconductors: this is more strong proof that the film quality of In_2O_3 can be improved via in-situ H doping in as-deposited films.

Table 2. The main electrical parameters and derived effective defect density of states for TFT devices.

	V_{th} (V)	μ_{FE} (cm^2/Vs)	$I_{\text{on}}/I_{\text{off}}$	SS (V/dec)	N_{eff} (cm^{-2}/eV)
0%-350	−15.0	37.8	2.83×10^7	0.52	1.82×10^{12}
3%-350	−5.2	45.6	5.94×10^8	0.27	9.46×10^{11}
5%-350	−4.1	47.8	7.20×10^8	0.25	8.76×10^{11}

4. Conclusions

In summary, polycrystalline In_2O_3 thin films and transistor devices were fabricated by room temperature magnetron sputtering with the introduction of H_2 into the working gas following an air annealing. Compared to the undoped one, the H-doped thin films show fewer defects (including oxygen vacancies and band-tail states) and a smoother surface morphology with similar average grain sizes. And the electron concentration obtained by Hall effect testing in the $\text{In}_2\text{O}_3:\text{H}$ films is approximately one order of magnitude lower than that in the undoped films, while the Hall mobility is enhanced. Regarding thin-film transistors, the threshold voltage gradually shifts toward the positive direction and the field-effect mobility increases with an increase in H_2 ratio, agreeing well with the variation trends for the thin films. And the improved subthreshold swing values indicate a reduction in defect states in $\text{In}_2\text{O}_3:\text{H}$ films. The optimized $\text{In}_2\text{O}_3:\text{H}$ TFT demonstrates markedly improved electrical performance, including a high field-effect mobility of $47.8 \text{ cm}^2/\text{Vs}$, a more positive threshold voltage, and a smaller subthreshold swing of 0.25 V/dec. These results supply a comprehensive investigation on the property evolutions for H-doped In_2O_3 thin films and their TFTs, which would provide an opportunity to boost their further exploration and application.

Supplementary Materials: The following supporting information can be downloaded at: <https://www.mdpi.com/article/10.3390/electronics13081478/s1>, Figure S1: (a) HAADF image and (b) EDS mapping results of the as-deposited $\text{In}_2\text{O}_3:\text{H}$ films at $R[\text{H}_2] = 5\%$.

Author Contributions: Conceptualization, L.L.; Methodology, L.L.; Software, P.H. and L.Y.; Formal analysis, P.H., Z.G. and W.L.; Investigation, Z.G. and X.L.; Data curation, T.L.; Writing—original draft, P.H.; Writing—review & editing, P.H.; Visualization, Y.Q.; Supervision, L.L., Y.H. and H.C.; Funding acquisition, H.C. All authors have read and agreed to the published version of the manuscript.

Funding: This project is supported by the National Key Research and Development Program of China (2021YFB3600701), the National Natural Science Foundation of China (62274167), the Key deployment project of the Chinese Academy of Sciences (ZDRW-XX-2022-2), the Natural Science Foundation of Zhejiang Province (LD21F040002) and the Innovation and Entrepreneurship Team of Zhejiang Province (2021R01003).

Data Availability Statement: Data are contained within the article and Supplementary Materials.

Conflicts of Interest: The authors declare no conflicts of interest.

References

1. Nomura, K.; Ohta, H.; Ueda, K.; Kamiya, T.; Hirano, M.; Hosono, H. Thin-Film Transistor Fabricated in Single-Crystalline Transparent Oxide Semiconductor. *Science* **2003**, *300*, 1269–1272. [[CrossRef](#)] [[PubMed](#)]
2. Kamiya, T.; Nomura, K.; Hosono, H. Present Status of Amorphous In–Ga–Zn–O Thin-Film Transistors. *Sci. Technol. Adv. Mater.* **2010**, *11*, 044305. [[CrossRef](#)] [[PubMed](#)]
3. Liang, L.; Zhang, H.; Li, T.; Li, W.; Gao, J.; Zhang, H.; Guo, M.; Gao, S.; He, Z.; Liu, F.; et al. Addressing the Conflict between Mobility and Stability in Oxide Thin-Film Transistors. *Adv. Sci.* **2023**, *10*, 2300373. [[CrossRef](#)]
4. Nomura, K.; Ohta, H.; Takagi, A.; Kamiya, T.; Hirano, M.; Hosono, H. Room-Temperature Fabrication of Transparent Flexible Thin-Film Transistors Using Amorphous Oxide Semiconductors. *Nature* **2004**, *432*, 488–492. [[CrossRef](#)] [[PubMed](#)]
5. Fortunato, E.; Barquinha, P.; Martins, R. Oxide Semiconductor Thin-Film Transistors: A Review of Recent Advances. *Adv. Mater.* **2012**, *24*, 2945–2986. [[CrossRef](#)] [[PubMed](#)]
6. Feneberg, M.; Nixdorf, J.; Lidig, C.; Goldhahn, R.; Galazka, Z.; Bierwagen, O.; Speck, J.S. Many-Electron Effects on the Dielectric Function of Cubic In₂O₃: Effective Electron Mass, Band Nonparabolicity, Band Gap Renormalization, and Burstein-Moss Shift. *Phys. Rev. B* **2016**, *93*, 045203. [[CrossRef](#)]
7. Yu, X.; Zeng, L.; Zhou, N.; Guo, P.; Shi, F.; Buchholz, D.B.; Ma, Q.; Yu, J.; Dravid, V.P.; Chang, R.P.H.; et al. Ultra-Flexible, “Invisible” Thin-Film Transistors Enabled by Amorphous Metal Oxide/Polymer Channel Layer Blends. *Adv. Mater.* **2015**, *27*, 2390–2399. [[CrossRef](#)] [[PubMed](#)]
8. Aikawa, S.; Nabatame, T.; Tsukagoshi, K. Effects of Dopants in InO_x-Based Amorphous Oxide Semiconductors for Thin-Film Transistor Applications. *Appl. Phys. Lett.* **2013**, *103*, 172105. [[CrossRef](#)]
9. Kim, W.-S.; Moon, Y.-K.; Kim, K.-T.; Shin, S.-Y.; Du Ahn, B.; Lee, J.-H.; Park, J.-W. The Influence of Hafnium Doping on Bias Stability in Zinc Oxide Thin Film Transistors. *Thin Solid Films* **2011**, *519*, 5161–5164. [[CrossRef](#)]
10. Xiao, P.; Dong, T.; Lan, L.; Lin, Z.; Song, W.; Song, E.; Sun, S.; Li, Y.; Gao, P.; Luo, D.; et al. High-Mobility Flexible Thin-Film Transistors with a Low-Temperature Zirconium-Doped Indium Oxide Channel Layer. *Phys. Status Solidi-Rapid Res. Lett.* **2016**, *10*, 493–497. [[CrossRef](#)]
11. Stewart, K.A.; Gouliouk, V.; Keszler, D.A.; Wager, J.F. Sputtered Boron Indium Oxide Thin-Film Transistors. *Solid-State Electron.* **2017**, *137*, 80–84. [[CrossRef](#)]
12. Kizu, T.; Aikawa, S.; Mitoma, N.; Shimizu, M.; Gao, X.; Lin, M.-F.; Nabatame, T.; Tsukagoshi, K. Low-Temperature Processable Amorphous In-W-O Thin-Film Transistors with High Mobility and Stability. *Appl. Phys. Lett.* **2014**, *104*, 152103. [[CrossRef](#)]
13. Zhang, H.; Liang, L.; Wang, X.; Wu, Z.; Cao, H. Praseodymium-Doped In-Sn-Zn-O TFTs with Effective Improvement of Negative-Bias Illumination Stress Stability. *IEEE Trans. Electron. Devices* **2022**, *69*, 152–155. [[CrossRef](#)]
14. Lan, L.; Li, X.; Ding, C.; Chen, S.; Su, H.; Huang, B.; Chen, B.; Zhou, H.; Peng, J. The Effect of the Charge Transfer Transition of the Tetravalent Terbium on the Photostability of Oxide Thin-Film Transistors. *Adv. Electron. Mater.* **2022**, *8*, 2200187. [[CrossRef](#)]
15. Liu, P.-T.; Chou, Y.-T.; Teng, L.-F.; Li, F.-H.; Shieh, H.-P. Nitrogenated Amorphous InGaZnO Thin Film Transistor. *Appl. Phys. Lett.* **2011**, *98*, 052102. [[CrossRef](#)]
16. Li, J.; Fu, Y.-Z.; Huang, C.-X.; Zhang, J.-H.; Jiang, X.-Y.; Zhang, Z.-L. Nitrogen Anion Doping as a Strategy to Suppress Negative Gate-Bias Illumination Instability of ZnSnO Thin Film Transistor. *Appl. Phys. Lett.* **2016**, *108*, 143505. [[CrossRef](#)]
17. Zhang, J.; Charnas, A.; Lin, Z.; Zheng, D.; Zhang, Z.; Liao, P.-Y.; Zemlyanov, D.; Ye, P.D. Fluorine-Passivated In₂O₃ Thin Film Transistors with Improved Electrical Performance via Low-Temperature CF₄/N₂O Plasma. *Appl. Phys. Lett.* **2022**, *121*, 172101. [[CrossRef](#)]
18. Kim, H.-D.; Kim, J.H.; Park, K.; Kim, J.H.; Park, J.; Kim, Y.J.; Kim, H.-S. Effects of Fluorine Doping on the Electrical Performance of ZnON Thin-Film Transistors. *ACS Appl. Mater. Interfaces* **2017**, *9*, 24688–24695. [[CrossRef](#)] [[PubMed](#)]
19. Kim, H.-D.; Naqi, M.; Jang, S.C.; Park, J.-M.; Park, Y.C.; Park, K.; Nahm, H.-H.; Kim, S.; Kim, H.-S. Nonvolatile High-Speed Switching Zn-O-N Thin-Film Transistors with a Bilayer Structure. *ACS Appl. Mater. Interfaces* **2022**, *14*, 13490–13498. [[CrossRef](#)]
20. Wardenga, H.; Frischbier, M.; Morales-Masis, M.; Klein, A. In Situ Hall Effect Monitoring of Vacuum Annealing of In₂O₃:H Thin Films. *Materials* **2015**, *8*, 561–574. [[CrossRef](#)]

21. Magari, Y.; Kataoka, T.; Yeh, W.; Furuta, M. High-Mobility Hydrogenated Polycrystalline In₂O₃ (In₂O₃:H) Thin-Film Transistors. *Nat. Commun.* **2022**, *13*, 1078. [[CrossRef](#)] [[PubMed](#)]
22. Ge, C.; Liu, Z.; Zhu, Y.; Zhou, Y.; Jiang, B.; Zhu, J.; Yang, X.; Zhu, Y.; Yan, S.; Hu, H.; et al. Insight into the High Mobility and Stability of In₂O₃:H Film. *Small* **2023**, *20*, 2304721. [[CrossRef](#)] [[PubMed](#)]
23. Koida, T. Amorphous and Crystalline In₂O₃-Based Transparent Conducting Films for Photovoltaics. *Phys. Status Solidi A-Appl. Mater.* **2017**, *214*, 1600464. [[CrossRef](#)]
24. Catalán, S.; Álvarez-Fraga, L.; Salas, E.; Ramírez-Jiménez, R.; Rodríguez-Palomo, A.; de Andrés, A.; Prieto, C. Charge Mobility Increase in Indium-Molybdenum Oxide Thin Films by Hydrogen Doping. *Appl. Surf. Sci.* **2016**, *386*, 427–433. [[CrossRef](#)]
25. Weiher, R.L.; Ley, R.P. Optical Properties of Indium Oxide. *J. Appl. Phys.* **1966**, *37*, 299–302. [[CrossRef](#)]
26. Girtan, M.; Rusu, G.I.; Rusu, G.G.; Gurlui, S. Influence of Oxidation Conditions on the Properties of Indium Oxide Thin Films. *Appl. Surf. Sci.* **2000**, *162*, 492–498. [[CrossRef](#)]
27. Addonizio, M.L.; Spadoni, A.; Antonaia, A.; Usatii, I.; Bobeico, E. Hydrogen-Doped In₂O₃ for Silicon Heterojunction Solar Cells: Identification of a Critical Threshold for Water Content and Rf Sputtering Power. *Sol. Energy Mater. Sol. Cells* **2021**, *220*, 110844. [[CrossRef](#)]
28. Krishna, B.R.; Subramanyam, T.K.; Naidu, B.S.; Uthanna, S. Effect of Substrate Temperature on the Electrical and Optical Properties of Dc Reactive Magnetron Sputtered Indium Oxide Films. *Opt. Mater.* **2000**, *15*, 217–224. [[CrossRef](#)]
29. Guo, S.; Diyatmika, W.; Unutulmazsoy, Y.; Yang, L.; Dai, B.; Xu, L.; Han, J.; Ralchenko, V.; Anders, A.; Zhu, J. High-Quality Transparent Conductive Indium Oxide Film Deposition by Reactive Pulsed Magnetron Sputtering: Determining the Limits of Substrate Heating. *Appl. Surf. Sci.* **2022**, *585*, 152604. [[CrossRef](#)]
30. Zhang, C.; Liu, G.; Geng, X.; Wu, K.; Debliquy, M. Metal Oxide Semiconductors with Highly Concentrated Oxygen Vacancies for Gas Sensing Materials: A Review. *Sens. Actuators A-Phys.* **2020**, *309*, 112026. [[CrossRef](#)]
31. Marwoto, P.; Khanifah, L.; Astuti, B.; Wibowo, E. Influence of Annealing Time on the Morphology and Oxygen Content of ZnO:Ga Thin Films. *J. Phys. Conf. Ser.* **2019**, *1321*, 022020. [[CrossRef](#)]
32. Medvedeva, J.E.; Sharma, K.; Bhattarai, B.; Bertoni, M.I. Hydrogen Behavior at Crystalline/Amorphous Interface of Transparent Oxide Semiconductor and Its Effects on Carrier Transport and Crystallization. *ACS Appl. Mater. Interfaces* **2022**, *14*, 39535–39547. [[CrossRef](#)] [[PubMed](#)]
33. Shi, J.; Zhang, J.; Yang, L.; Qu, M.; Qi, D.-C.; Zhang, K.H.L. Wide Bandgap Oxide Semiconductors: From Materials Physics to Optoelectronic Devices. *Adv. Mater.* **2021**, *33*, 2006230. [[CrossRef](#)] [[PubMed](#)]
34. He, J.; Li, G.; Lv, Y.; Wang, C.; Liu, C.; Li, J.; Flandre, D.; Chen, H.; Guo, T.; Liao, L. Defect Self-Compensation for High-Mobility Bilayer InGaZnO/In₂O₃ Thin-Film Transistor. *Adv. Electron. Mater.* **2019**, *5*, 1900125. [[CrossRef](#)]
35. Wang, H.; He, J.; Xu, Y.; Andre, N.; Zeng, Y.; Flandre, D.; Liao, L.; Li, G. Impact of Hydrogen Dopant Incorporation on InGaZnO, ZnO and In₂O₃ Thin Film Transistors. *Phys. Chem. Chem. Phys.* **2020**, *22*, 1591–1597. [[CrossRef](#)]
36. Li, W.; Yang, L.; Gao, Z.; Ren, J.; Hu, P.; Li, T.; Liang, L.; Cao, H. Impact of the Source/Drain Electrode Process on the Mobility-Threshold Trade-Off for InSnZnO Thin-Film Transistors. *ACS Appl. Electron. Mater.* **2023**, *5*, 1615–1619. [[CrossRef](#)]
37. Kamiya, T.; Nomura, K.; Hosono, H. Electronic Structures Above Mobility Edges in Crystalline and Amorphous In-Ga-Zn-O: Percolation Conduction Examined by Analytical Model. *J. Disp. Technol.* **2009**, *5*, 462–467. [[CrossRef](#)]
38. Nakata, M.; Zhao, C.; Kanicki, J. DC Sputtered Amorphous In-Sn-Zn-O Thin-Film Transistors: Electrical Properties and Stability. *Solid-State Electron.* **2016**, *116*, 22–29. [[CrossRef](#)]

Disclaimer/Publisher's Note: The statements, opinions and data contained in all publications are solely those of the individual author(s) and contributor(s) and not of MDPI and/or the editor(s). MDPI and/or the editor(s) disclaim responsibility for any injury to people or property resulting from any ideas, methods, instructions or products referred to in the content.